

# Interplay of growth mode and thermally induced spin accumulation in epitaxial Al/Co<sub>2</sub>TiSi/Al and Al/Co<sub>2</sub>TiGe/Al contacts

Benjamin Geisler,<sup>1</sup> Peter Kratzer,<sup>1</sup> and Voicu Popescu<sup>1,\*</sup>

<sup>1</sup> Faculty of Physics and Center for Nanointegration (CENIDE),  
University of Duisburg-Essen, Lotharstraße 1, 47057 Duisburg, Germany

(Dated: February 19, 2014)

The feasibility of thermally driven spin injectors built from half-metallic Heusler alloys inserted between aluminum leads was investigated by means of *ab initio* calculations of the thermodynamic equilibrium and electronic transport. We have focused on two main issues and found that: (i) the interface between Al and the closely lattice-matched Heusler alloys of type Co<sub>2</sub>TiZ (Z = Si or Ge) is stable under various growth conditions; and (ii) the conventional and spin-dependent Seebeck coefficients in such heterojunctions exhibit a strong dependence on both the spacer and the atomic composition of the Al/Heusler interface. The latter quantity gives a measure of the spin accumulation and varies between +8  $\mu\text{V/K}$  and -3  $\mu\text{V/K}$  near 300 K, depending on whether a Ti-Ge or a Co-Co plane makes the contact between Al and Co<sub>2</sub>TiGe in the trilayer. Our results show that it is in principle possible to tailor the spin-caloric effects by a targeted growth control of the samples.

PACS numbers: 72.10.-d, 72.15.Jf, 73.50.Jt

## I. INTRODUCTION

A central topic of spintronics is the design and realization of spin injectors.<sup>1</sup> These are contacts that allow one to induce a spin accumulation (or, in general terms, an imbalance of the chemical potential for the two spin channels) in a substrate that typically consists of a conventional, technologically standard semiconductor such as silicon.<sup>2</sup> Their practical realization, on the other hand, can be hindered by various factors.

Indeed, while the spin injection may in principle be accomplished using magnetic transition metals and their alloys, the preparation of an atomically well-defined interface between a transition metal and the Si surface is very difficult due to the high tendency of exothermic silicide formation.<sup>3-7</sup> As an alternative one could use a light *sp*-metal such as aluminum as a contact layer between Si and the ferromagnetic layer. Ohmic contacts between Si and Al are well-studied and form a standard component in Si device technology.<sup>8</sup> More importantly, aluminum displays a very large spin diffusion length,<sup>9</sup> and hence Al leads are suitable to conduct a spin-polarized current without substantial losses. The problem is then rendered into finding an appropriately matching ferromagnetic system acting as spin injector.

For this task, the ferromagnetic full Heusler alloys have been recently investigated theoretically as promising candidates.<sup>10</sup> In their ideal  $L2_1$  crystal structure bulk phase these systems exhibit a half-metallic behavior,<sup>11</sup> which in principle may allow a high degree of spin polarization of the injected current. Moreover, as shown in Fig. 1(a), the  $L2_1$  structure can be matched by an Al structure rotated by 45° about the  $z$ -axis. In particular, the Co-based full Heusler alloys Co<sub>2</sub>TiSi or Co<sub>2</sub>TiGe recommend themselves for integrated spin injectors in combination with an Al contact layer as the experimentally determined lattice mismatch is small (less than  $\simeq 2\%$ ).

Applying an external voltage to a Heusler/Al/Si junction may not be, however, the best way to achieve a high value of spin accumulation. A considerable obstacle in the practical realization of a metal-semiconductor spin injector is the so-called conductivity mismatch<sup>12</sup> between the different materials. This leads to a potential drop in locations where it is not useful for the device, while the spin accumulation in the semiconductor itself might remain small. It has been suggested<sup>13</sup> that this difficulty could be overcome by applying an external temperature gradient, rather than an external voltage, in order to induce the spin accumulation: Exploiting the Seebeck effect, a temperature gradient across the contact directly results in a difference in the chemical potentials in the two spin channels due to the spin-dependence of the Seebeck coefficient. This difference is independent of an injected current and hence unaffected by a possible mismatch in conductivity. Experimental studies<sup>14,15</sup> on bulk samples have shown that the Ti-based Heusler alloys, such as Co<sub>2</sub>TiSi or Co<sub>2</sub>TiGe, display large Seebeck voltages under an applied temperature gradient. One would expect from these findings that these materials, in conjunction with their half-metallic electronic structure, might also show a large *spin*-dependence of the Seebeck coefficient, thus making them suitable candidates for spin injectors based on spin-caloric effects.

Motivated by the issues listed above, it is the aim of our present investigations to assess the ability of Al/Co<sub>2</sub>TiZ/Al (Z = Si, Ge) trilayers to serve as thermally driven spin injectors. This has been accomplished by performing first-principles calculations of the electronic structure and of the thermoelectric transport properties. While neglecting the other side of the device, the spin injector-semiconductor contact, we focused on two specific problems for the Al/Co<sub>2</sub>TiZ/Al systems: (i) stability and electronic structure of the Al/Heusler interface, and (ii) whether they open a promising path towards

maximizing the thermal induced spin accumulation. We further provide a detailed insight in the electronic transport mechanisms in these junctions, accounting for a realistic morphology of the interface and focusing on the electronic structure contribution to the transmission and Seebeck coefficient.

Our results show that the formation energy of the Al/Heusler interface is negative, which means that these interfaces are stable. While both Heusler alloys can match the Al substrate either with a Ti-Z or a Co-Co atomic plane, the former needs non-equilibrium growth conditions to avoid the formation of competing TiZ compounds. We find that the spin-dependent Seebeck effect is sensitive precisely to this atomic structure of the Al/Heusler interface. In particular, for a thin  $\text{Co}_2\text{TiSi}$  or  $\text{Co}_2\text{TiGe}$  layer terminated by a Ti-Si or Ti-Ge plane, the spin-dependent Seebeck coefficient is positive and of the same order of magnitude as the conventional, spin-averaged Seebeck coefficient. For a Co-Co terminated Al/ $\text{Co}_2\text{TiGe}$ /Al trilayer both coefficients are negative. This suggests the possibility of achieving a large and stable spin accumulation by appropriate growth conditions.

## II. DESCRIPTION OF STRUCTURES AND APPLIED METHODS

### A. Setting up the Al/Heusler/Al trilayer system

At the center of our investigations are the Al/ $\text{Co}_2\text{TiZ}$ /Al junctions in trilayer geometry, with  $Z = \text{Si}$  or  $\text{Ge}$ . We give here the geometric arguments for the feasibility of such heterostructures and will show later by first principles calculations that they are energetically stable. The  $\text{Co}_2\text{TiZ}$  compounds belong to the class of full Heusler alloys<sup>16</sup> of type  $X_2YZ$  which crystallize in the cubic  $L2_1$  structure. This crystal structure, depicted in Fig. 1(a), has a face-centered-cubic (fcc) primitive cell with four inequivalent atomic sites. It is usually described as four inter-penetrating fcc sublattices respectively occupied by the  $X$ ,  $Y$ ,  $X$ , and  $Z$  atoms, shifted against each other by  $(a/4, a/4, a/4)$ , with  $a$  the cubic lattice constant. Alternatively, one can represent the  $L2_1$  structure by two inter-penetrating  $XY$  and  $XZ$  zinc-blende structures, with the latter shifted by  $(0, 0, a/2)$ . Aluminum, on the other hand, possesses the simple  $A1$  crystal structure, consisting of an fcc Bravais lattice with one atom per unit cell. As illustrated in Fig. 1(a), the  $A1$  structure, rotated by 45 degrees about the  $z$  axis, represents a natural continuation of the  $L2_1$  structure, enabling a perfect epitaxial match of the two systems if their lattice constants are in a ratio of  $a(L2_1)/a(A1) = \sqrt{2}$ . The two Heusler alloys chosen for the present study deviate only slightly from this condition, namely by 1.07 % for  $\text{Co}_2\text{TiSi}/\text{Al}$  and 2.70 % for  $\text{Co}_2\text{TiGe}/\text{Al}$ .

Bringing together the two structures, on the other hand, requires the use of a tetragonal unit cell of in-

plane lattice constant  $a_{\text{tet}} = a(A1)$ , with unit vectors oriented along the  $L2_1$ -(110) and  $(\bar{1}10)$  directions, and of varying length  $c$  along the common (001) direction. Each plane of the tetragonal unit cell contains two inequivalent atomic sites. The Al/ $\text{Co}_2\text{TiZ}$  heterostructures were modeled with such supercells with  $a_{\text{tet}}$  fixed to the equilibrium lattice constant of Al metal. We considered two terminations of the Heusler materials at the interface to the Al electrodes: a pure Co-Co layer and a mixed Ti-Z layer, where  $Z = \text{Si}$  or  $\text{Ge}$ , as illustrated in Fig. 1(b) and (c). The supercells contain  $2 \times 10$  Al planes and  $8 + 7$  Co (Ti-Z) and Ti-Z (Co) Heusler planes, leading to an appropriate, well-converged potential in the Al electrodes. We constructed the supercells such that the Heusler atoms simply continue the Al fcc lattice by occupying the hollow sites next to the interface.

All internal atomic positions have been accurately optimized using Hellmann-Feynman forces to reduce the force components below 1 mRy/bohr and the energy changes below 0.1 mRy. Moreover, the length of the tetragonal Al/Heusler/Al supercells has been optimized for each considered structure in order to determine the ideal, energy minimizing Al-Heusler spacing.

### B. Electronic structure calculations

The electronic structure and transport calculations have been performed within the framework of spin-polarized density functional theory (DFT) employing the plane-wave pseudopotential method as implemented in the Quantum Espresso code,<sup>17</sup> with the PBE<sup>18</sup> generalized gradient approximation (GGA) parametrization of the exchange-correlation functional. Wave functions and density have been expanded into plane waves up to cutoff energies of 40 Ry and 400 Ry, respectively. The neighborhood of atom centers has been approximated by self-created ultrasoft pseudopotentials (USPPs),<sup>19</sup> treating the atomic Si 3s, 3p, Ge 3d, 4s, 4p, Co 3d, 4s, 4p, and Ti 3s, 3p, 3d, 4s, 4p subshells as valence states.<sup>20</sup> For Si, Ge, and Co a non-linear core correction<sup>21</sup> was included. In the pseudopotential creation process a scalar relativistic approximation was applied to the electron motion. A Methfessel-Paxton smearing<sup>22</sup> of 10 mRy has been applied to the Brillouin zone sampling performed with different Monkhorst-Pack  $k$ -point grids:<sup>23</sup> For the Heusler fcc bulk calculations, we used a  $16 \times 16 \times 16$  grid;  $20 \times 20 \times 14$  for the tetragonal Heusler cells and  $20 \times 20 \times 20$  for the Al cubic cell. Finally, for the Al/Heusler/Al supercells the  $k$ -point grid was  $16 \times 16 \times 4$ . All grids were chosen in such a way that they did not include the  $\Gamma$  point and deliver accurately converged Fermi energies and potentials. Post-processing of densities of states was performed with much denser  $k$ -point grids that included the  $\Gamma$  point.

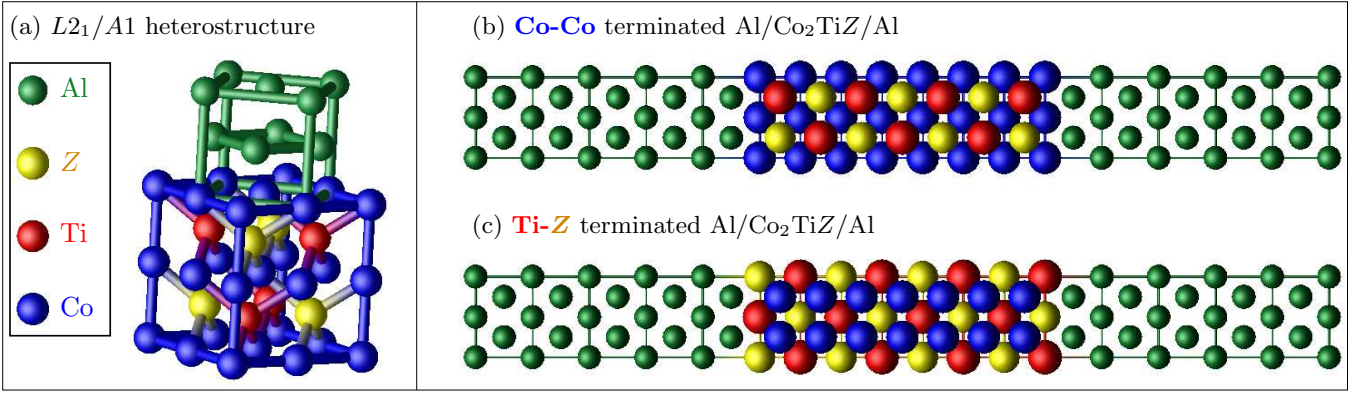


FIG. 1: (Color online) (a) Structural model of the  $Co_2TiZ$  ( $Z=Si/Ge$ ) full Heusler  $L_{21}$  structure matched to the Al  $Al_1$  structure rotated by an angle of 45 degrees about the vertical ( $z$ ) axis. Panels (b) and (c) show (110)-projected views of the tetragonal  $Al/Co_2TiZ/Al$  supercells used in our calculations with either Co-Co or Ti-Z termination of the Al/Heusler interface.

### C. Interface formation energies

Based on the results obtained for the constructed supercells it is possible, using an *ab initio* thermodynamic approach,<sup>24</sup> to derive interface energies,

$$\gamma(\mu_{Co}) = \frac{1}{2A} [E_{sc} - N_{Al}E_{Al} - \mu_{Co}(N_{Co} - 2N_Z) - N_Z E_{Co_2TiZ}] , \quad (1)$$

which provide information about the stability of different interfaces in thermodynamic equilibrium. Here  $E_{sc}$ ,  $E_{Al}$ , and  $E_{Co_2TiZ}$  are the DFT total energies of the considered supercell, Al bulk, and the respective Heusler bulk;  $A$  is the interface area and the  $N_i$ 's denote the different numbers of atoms of species  $i$  in the supercell. Corrections to the interface energy as they arise, for instance, due to the phonon free energy at finite temperatures are neglected, since they will certainly be similar for the different structures. In writing down this expression, one considers Co, Ti, and Z to be in equilibrium with the bulk phase of  $Co_2TiZ$ :

$$E_{Co_2TiZ} = 2\mu_{Co} + \mu_{Ti} + \mu_z . \quad (2)$$

In addition, for the supercells considered here, the interface energy explicitly depends only on  $\mu_{Co}$ , since in all cases  $N_{Ti} = N_Z$ . A reduced chemical potential  $\tilde{\mu}_{Co} = \mu_{Co} - E_{Co}$  can be defined using the DFT energy of hcp Co,  $E_{Co}$ . Since this quantity corresponds to the formation of the Co metal, the inequality

$$\tilde{\mu}_{Co} \leq 0 \quad (3)$$

can be seen as an upper bound of the reduced chemical potential of Co. Different lower bounds can be determined by taking into account the formation of competing compounds such as CoTi, TiZ. Assuming, for example, Co and Ti to be in equilibrium with the CoTi bulk phase,

$$E_{CoTi} = \mu_{Co} + \mu_{Ti} , \quad (4)$$

it follows, using Eq. (2),

$$E_{Co_2TiZ} - E_{CoTi} \leq \mu_{Co} + \mu_z \quad (5)$$

or

$$\tilde{\mu}_{Co} \geq -\tilde{\mu}_z + [E_{Co_2TiZ} - E_{CoTi} - E_{Co} - E_z] , \quad (6)$$

where, except for the parameter  $\tilde{\mu}_z = \mu_z - E_z$ , all quantities on the rhs are directly accessible from DFT calculations for the corresponding systems. Other lower boundaries for  $\tilde{\mu}_{Co}$  can be determined analogously.

### D. Calculation of Seebeck coefficients

For the transport properties we considered an open quantum system consisting of a scattering region comprising the Heusler material and interfaces to the electrode material, and left and right semi-infinite electrodes. From the accurately converged DFT potentials of the leads and the scattering regions, transport coefficients have been calculated separately for both spin channels using a method following Refs. 25 and 26. In order to sample the two-dimensional Brillouin zone on a reasonable computational time scale, we have massively parallelized the method. Convergence of the energy- and spin-resolved transmission probability  $\mathcal{T}_\sigma(E)$ ,

$$\mathcal{T}_\sigma(E) = \frac{1}{A_{BZ}} \int d^2k_{\parallel} \mathcal{T}_\sigma(\vec{k}_{\parallel}, E), \quad (7)$$

with respect to the  $k_{\parallel}$ -point grid has been found to be attained with a  $201 \times 201$   $k_{\parallel}$ -points regular mesh. The Seebeck coefficients have been evaluated using the approach of Sivan and Imry<sup>27</sup> starting from the central quantity  $\mathcal{T}_\sigma(E)$  and the Fermi occupation function  $f_0(E, T, \mu)$ . Within Mott's two current model the spin-projected conductance is expressed as

$$G_\sigma(T) = -\frac{e^2}{h} \int dE \frac{\partial f_0}{\partial E} \mathcal{T}_\sigma(E) , \quad (8)$$

while the spin-projected Seebeck coefficient takes on the form

$$S_{\sigma}(T) = -\frac{1}{eT} \frac{\int dE \frac{\partial f_0}{\partial E} (E - E_F) \mathcal{T}_{\sigma}(E)}{\int dE \frac{\partial f_0}{\partial E} \mathcal{T}_{\sigma}(E)} . \quad (9)$$

Using the two quantities above the effective (also called charge) Seebeck coefficient can be expressed as

$$S_{\text{eff}} = \frac{G_{\uparrow} S_{\uparrow} + G_{\downarrow} S_{\downarrow}}{G_{\uparrow} + G_{\downarrow}} , \quad (10)$$

and the spin-dependent Seebeck coefficient by the formula

$$S_{\text{spin}} = \frac{G_{\uparrow} S_{\uparrow} - G_{\downarrow} S_{\downarrow}}{G_{\uparrow} + G_{\downarrow}} , \quad (11)$$

with the temperature argument  $T$  omitted. The energy integration in Eqs. (8) and (9) consists of two steps: An explicit calculation of  $\mathcal{T}_{\sigma}(E)$  on a regular  $E$  mesh with a 15 meV spacing followed by an interpolation of  $\mathcal{T}_{\sigma}(E)$  on a refined  $E$  mesh with a 1.36 meV (0.1 mRy) spacing.

The formalism adopted here to calculate the transport properties only considers elastic scattering of the electrons by the interfaces, whereas inelastic scattering processes, e.g., by phonons or spin fluctuations, are neglected. For high temperatures these scattering mechanisms are expected to become more and more important. For example, including the electron scattering by spin fluctuations in various ferromagnetic metals and alloys had lead to a better agreement of the temperature dependent resistivity with experimental data.<sup>28,29</sup> A more recent study<sup>30</sup> investigated the effect of spin disorder on the magneto-thermoelectric phenomena in nano-structured Co systems. It could be demonstrated that, while the spin-dependent electron scattering does indeed influence the spin-caloric transport coefficients at high temperatures, this influence is strongly case dependent, such that no actual quantitative or qualitative predictions can be made, without an explicit calculation. For this reason, we restrict our investigations to a temperature range below 350 K and assume that, owing to the fair similar electronic structure of the investigated systems, the trends determined only on the basis of the electronic contribution are quite reliable.

### III. GROUND STATE PROPERTIES OF BULK CO<sub>2</sub>TiSi AND CO<sub>2</sub>TiGe

#### A. Results for the cubic $L2_1$ phase

The electronic, magnetic, and transport properties of the *bulk* Co<sub>2</sub>TiZ Heusler alloys (with  $Z$  being a group IV element) are well documented in the literature.<sup>11,15,31,32</sup> We particularly refer the reader to the systematic study presented by Barth *et al.*<sup>15</sup> which combines full-potential

LAPW-based theoretical investigations with various experimental observations and provides a quite exhaustive overview of the various properties of the Co<sub>2</sub>TiZ system. We use their all-electron results to assess the quality of our pseudopotential approach. Table I gives the results of total energy minimizations for Co<sub>2</sub>TiSi and Co<sub>2</sub>TiGe with the equilibrium lattice constant  $a$  and bulk modulus  $B$  obtained from a fit to the Birch-Murnaghan equation of state. A comparison with the theoretical and experimental literature data evidences the excellent agreement with previous GGA-PBE results which are, in turn, only a few percent off the experimentally determined lattice constants.

System	Lattice constants		$B$ (GPa)	Source
	$a$ (Å)	$c$ (Å)		
Co <sub>2</sub> TiSi $L2_1$	5.756		204	present work
	5.753		210	Theory <sup>31</sup>
	5.758		207	Theory <sup>15</sup>
	5.74			Experiment <sup>33,34</sup>
	5.849			Experiment (300 K) <sup>15</sup>
Co <sub>2</sub> TiGe $L2_1$	5.848		189	present work
	5.842		193	Theory <sup>31</sup>
	5.850		190	Theory <sup>15</sup>
	5.83(1)			Experiment <sup>33,34</sup>
	5.820			Experiment (300 K) <sup>15</sup>
Co <sub>2</sub> TiSi epi	5.695	5.819	290	present work
Co <sub>2</sub> TiGe epi	5.695	6.056	234	present work

TABLE I: Calculated ground-state equilibrium lattice constants and bulk moduli of the Heusler alloys Co<sub>2</sub>TiSi and Co<sub>2</sub>TiGe. The results are given for the cubic  $L2_1$  phase as well as for the tetragonally distorted structure with a fixed in-plane lattice constant  $a(L2_1) = a_0\sqrt{2}$ , which corresponds to Heusler alloys epitaxially grown on fcc-Al(001) of lattice constant  $a_0 = 4.027$  Å. The results for the cubic systems are compared with available theoretical and experimental literature data.

In their paper, Barth *et al.*<sup>15</sup> characterize the Co<sub>2</sub>TiZ compounds as itinerant ferromagnetic half-metals and contrast their behavior to that of other Co-based Heusler alloys that have late 3d metals, e.g. Mn or Fe, on the  $Y$  position. In addition, the samples prepared are reported to have nearly ideal 2 : 1 : 1 stoichiometry and magnetic moments of 1.96  $\mu_B$  for Co<sub>2</sub>TiSi and 1.94  $\mu_B$  for Co<sub>2</sub>TiGe. These combined results appear to hint towards the half-metallicity of these systems as well as the absence of substitutional (also called native) disorder between the four fcc sublattices that has been shown to influence significantly the anomalous Hall coefficient in several Heusler compounds.<sup>35</sup>

We show in Fig. 2 the spin-resolved partial and total density of states (DOS) curves for Co<sub>2</sub>TiSi and Co<sub>2</sub>TiGe calculated at their respective equilibrium lattice constants. This figure clearly demonstrates the half-metallic

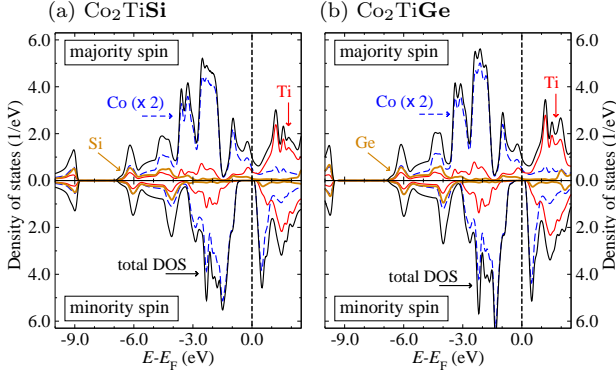
Co<sub>2</sub>TiZ in the  $L_{21}$  phase at equilibrium lattice constant

FIG. 2: (Color online) Spin-polarized total and partial density of states of (a) Co<sub>2</sub>TiSi and (b) Co<sub>2</sub>TiGe as calculated for their cubic  $L_{21}$  phase at the corresponding equilibrium lattice constants given in Table I.

character of both systems with the Fermi energy lying close to the upper edge of the band gap appearing in the minority spin channel. The width of this gap, estimated from the calculated band structure (see below) is 0.834 eV for Co<sub>2</sub>TiSi and 0.636 eV for Co<sub>2</sub>TiGe. Our results shown in Fig. 2, which are again in very good agreement with those obtained by other authors,<sup>15,32</sup> further evidence that the 3d states of Ti (red/light gray lines) are almost completely empty and that the spin magnetic moment of 2  $\mu_B$  found in these systems stems exclusively from the two Co atoms (dashed blue/dark gray lines). We have performed a series of calculations with a step-wise increase of the Fermi smearing to mimic the increase of the *electronic* temperature. It was found that the total magnetization remains unchanged up to a value of 600 K, much higher than the measured Curie temperature in these compounds, which lies around 380 K.<sup>15</sup>

### B. Free standing epitaxial Heusler alloys on Al(001)

The concept of a free standing epitaxial system designates a partially constrained geometry in which the in-plane lattice constant is fixed, typically to that of a substrate. Along the perpendicular direction, both atomic and unit cell parameter relaxation is allowed to occur in order to minimize the total energy. In such a setup, no actual interaction with the substrate is accounted for, isolating this way the effect of the epitaxial biaxial strain on the electronic structure of the material under investigation. We present in this section results of such calculations for the two Heusler systems Co<sub>2</sub>TiSi and Co<sub>2</sub>TiGe and will use them later as reference for the actual Al/Heusler/Al trilayers.

We describe the epitaxial Heusler alloys by tetragonal structures with a lattice constant  $a_0 = 4.027$  Å, corresponding to the GGA-PBE equilibrium value for Al ob-

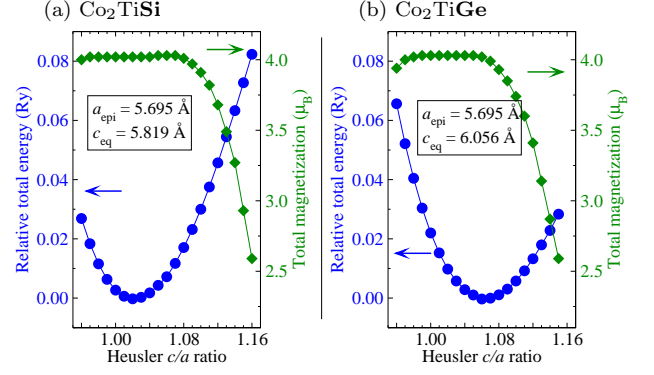
Free standing epitaxial Co<sub>2</sub>TiZ on fcc-Al(001)

FIG. 3: (Color online) Relative total energy with respect to its minimum (circles, left side axis) and total magnetization (diamonds, right side axis) for the tetragonally distorted (a) Co<sub>2</sub>TiSi and (b) Co<sub>2</sub>TiGe with a fixed in-plane lattice constant  $a_0 = 4.027$  Å. The inset gives the equilibrium parameters in the appropriately distorted  $L_{21}$  structure.

tained from the used pseudopotential. The corresponding  $L_{21}$  lattice constant is  $a_{\text{epi}}(L_{21}) = a_0\sqrt{2} = 5.695$  Å, which has to be compared with the equilibrium lattice constants of the cubic  $L_{21}$  structure given in Table I. Since  $a_{\text{epi}}(L_{21})$  is smaller than  $a(L_{21})$  for both systems (1.07 % and 2.70 % mismatch, respectively), the epitaxial matching is expected to produce a compressive strain which leads to a tetragonal distortion with a  $c/a(L_{21})$  ratio larger than one.

The results are summarized in Fig. 3 where we show the total energy (left side axis) and total magnetization (right side axis) for (a) Co<sub>2</sub>TiSi, and (b) Co<sub>2</sub>TiGe. The calculated equilibrium  $c/a(L_{21})$  ratios are 1.022 for Co<sub>2</sub>TiSi and 1.063 for Co<sub>2</sub>TiGe. These values are, as expected, larger than one, and consistent with the larger mismatch and the smaller bulk modulus  $B$  of Co<sub>2</sub>TiGe. We also note that the individual atomic displacements during the internal relaxation did not exceed  $10^{-3}$  Å with respect to the symmetric positions, preserving an equally spaced  $c/4$  vertical stacking.

From Fig. 3 it is also evident that both materials remain half-metallic (the total magnetization is  $\simeq 1.00$   $\mu_B/\text{Co}$  atom) over a broad range of  $c/a(L_{21})$  ratios. Moreover, the drop in the total magnetization occurs *above* the  $c/a(L_{21})$  equilibrium ratio. The preservation of half-metallicity at relatively large tetragonal distortions will prove to be an important result in view of the transport properties of the Al/Heusler/Al trilayers.

We have to emphasize here that, since we considered a single in-plane lattice constant, the attained minimum of the total energy should not be understood as a proof for the existence of a stable tetragonal structure for the considered Heusler alloys. In fact, Meinert *et al.*<sup>36</sup> performed total energy calculations for the isoelectronic system Co<sub>2</sub>TiSn over a series of in-plane lattice constants. In the absence of an epitaxial constraint, no tetragonal

structure was found to have smaller total energy than the cubic  $L2_1$  structure.

The effect of the biaxial strain on the band structure of the  $\text{Co}_2\text{TiZ}$  is significant, and the way in which the individual bands are affected is non-trivial. We illustrate this in Fig. 4 for the  $\text{Co}_2\text{TiGe}$  Heusler alloy. Qualitative similar features were found also for  $\text{Co}_2\text{TiSi}$ . In this case, however, the biaxial strain is smaller and the corresponding effects on the band structure are weaker.

Figure 4 shows the spin-resolved dispersion relations  $E(\vec{k})$ , with the two panels, left and right, displaying respectively the majority and minority spin bands. For each spin, the bands stemming from the two structures,  $L2_1$  and epitaxial tetragonal, are put together in the same frame. In both cases the band structure calculations employed a tetragonal unit cell of similar construction as above, with lattice constants adopted to recover the appropriate geometry. Adopting a Bravais lattice of the same symmetry has the advantage of dealing with identical *folding* of the bands, which allows one to directly isolate those changes that are solely due to the biaxial strain. Further comparison with band structure literature data<sup>15,32</sup> is possible, but demanding.<sup>37</sup>

The  $E(\vec{k})$  relations are represented in Fig. 4 for several directions in the Brillouin zone (BZ) for which only the  $k_z$  component of  $\vec{k}$  varies, while  $k_x$  and  $k_y$  are fixed:  $\Gamma$ - $Z$ ,  $X$ - $R$ , and  $M$ - $A$ . The notation used here corresponds to the tetragonal BZ.<sup>38</sup> In addition, the band structure is shown over a small energy interval, 3 eV wide, around the Fermi energy  $E_F$ . Its value, different in the two phases, is taken here as reference. This choice, while still enabling the strain effect analysis, will also prove useful when discussing the electronic transmission probability in the Al/Heusler/Al trilayers.

For the cubic  $L2_1$  structure [thin light blue (grey) lines Fig. 4] just a single band crosses the Fermi energy in the majority spin channel (left panel). This band is accompanied by its fcc-folded pair, particularly evident along the  $\Gamma$  -  $Z$  and  $M$  -  $A$  directions. Most of the majority spin bands in the chosen energy interval are highly dispersive. Several localized Co  $d$  bands can be observed, e.g. the flat bands at -0.3 eV and -1.5 eV along  $\Gamma$  -  $Z$  and around -1.0 eV along  $M$  -  $A$ . The bands of the epitaxial tetragonal  $\text{Co}_2\text{TiGe}$  [thick dark red (grey) lines] are shifted in energy against that of the cubic system but each by a different amount. While all the  $d$  bands appear to move towards higher energies under biaxial strain, the shift of the  $s$  and  $p$  bands depends both on energy and on  $\vec{k}$ . For example, the spin-up band crossing  $E_F$  along  $M$  -  $A$  is hardly affected by the tetragonal distortion, whereas the one right below it is found much lower in energy than its  $L2_1$  counterpart. A close inspection of the other panels, e.g., below  $E_F$  along  $\Gamma$  -  $Z$ , reveals similar characteristics, indicating a non-rigid band structure shift under biaxial strain.

Similar changes of the band structure with the tetragonal distortion are also observed in the minority spin channel (right panel). Here the most striking feature is

how the band gap in this spin channel – the landmark of half-metallicity – strongly diminishes under epitaxial strain. It can be seen, in fact, that the ‘minority conduction band’ in epitaxial  $\text{Co}_2\text{TiGe}$  nearly touches the Fermi energy along  $M$  -  $A$  direction, while the ‘valence band’ is practically pinned relative to  $E_F$ . This provides the explanation for the drop in the total magnetization evidenced in Fig. 3: Since with increasing height of the tetragonal cell the minority spin band gap gets narrower and it plunges below the Fermi energy, the system becomes metallic. Note that the tetragonal distortion of epitaxial  $\text{Co}_2\text{TiSi}$  at equilibrium is less pronounced and, as a consequence, the minority spin band gap reduction is smaller in this case.

We will investigate in the next section the Al/Heusler interface and will show that, within few monolayers away from it, the Heusler alloys stabilize into a tetragonal structure of identical geometry as determined here for the free standing system. One can therefore regard the Al/Heusler/Al trilayer systems as comprising a tetragonally distorted Heusler alloy spacer. The band structure features discussed here have an important influence on the transport properties of the whole junction; for example, the minority-spin band gap reduction is equivalent to a lowering of the potential barrier for spin-down electrons.

#### IV. STABILITY AND PROPERTIES OF THE AL/CO<sub>2</sub>TiZ INTERFACE

The matching of Al(001) and  $\text{Co}_2\text{TiZ}$  Heusler alloys in a heterostructure appears justified by the morphology considerations made above. Our arguments were based so far on the atomic arrangement and the small lattice mismatch between the two systems. We will show in this section by means of *ab initio* thermodynamics that the Al/ $\text{Co}_2\text{TiZ}$  ( $Z = \text{Si}, \text{Ge}$ ) interfaces, both with Co-Co and Ti-Z terminations, have a negative formation energy and are thus stable against Al and  $\text{Co}_2\text{TiZ}$  separation. The stabilization of Ti-Z terminated interfaces, however, requires non-equilibrium growth conditions because of the competing formation of TiZ compounds. In addition, we find that within a short distance away from the interface the Heusler systems take on the epitaxial geometry discussed in the preceding section, with a preserved half-metallicity reflected in the electronic structure. Such a fast transition to the half-metallic state appears to be an ubiquitous characteristic of the Heusler-based interfaces, whether they contain other Heusler alloys<sup>10</sup>, semiconductors like Si,<sup>5</sup> or insulators like MgO.<sup>39</sup>

##### A. Stability of the interface

We describe the interfaces in our calculations using the tetragonal supercells depicted in Fig. 1(b) and (c), assuming that the Al fcc substrate lattice can be contin-



$$E(\vec{k}) \text{ in } \text{Co}_2\text{TiGe} - L_{21} \text{ phase versus epitaxial on Al(001)}$$

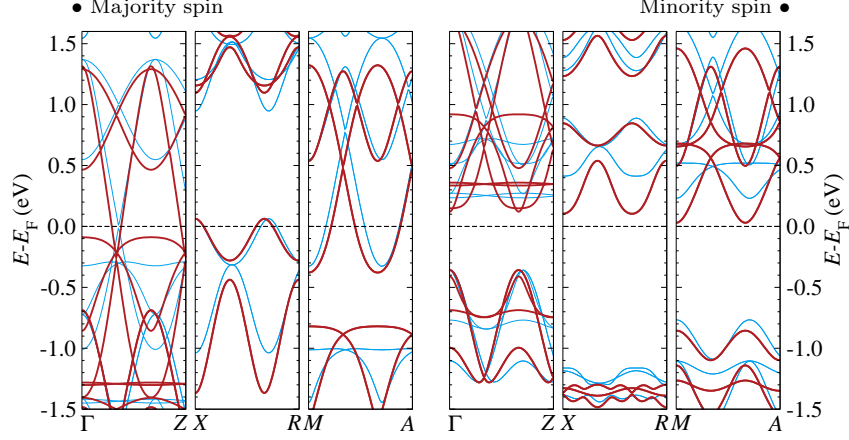


FIG. 4: (Color online) Comparison of the spin-resolved band structure [majority (minority) spin in the left (right) panel] calculated for the Heusler alloy  $\text{Co}_2\text{TiGe}$  in the equilibrium  $L_{21}$  phase [thin light blue (grey) lines] versus that of the tetragonally distorted Al(001)-matched structure [thick dark red (grey) lines]. Both calculations were done using a tetragonal unit cell to which the notation of the high-symmetry points in the BZ refers. Note that for each selected direction only the  $k_z$  component of the wavevector varies, while  $k_x$  and  $k_y$  are fixed.

ued either by Ti and Z atoms ( $Z = \text{Si/Ge}$ ), or by two Co atoms. Based on total energy calculations including structural relaxation, we calculate the interface energy as a function of the reduced chemical potential of Co,  $\tilde{\mu}_{\text{Co}} = \mu_{\text{Co}} - E_{\text{Co}}$ , according to Section II C.

The results of our calculations are displayed in Fig. 5(a) and (b). Each panel shows two lines corresponding to the Ti-Z and Co-Co termination of the respective interface, Al/ $\text{Co}_2\text{TiSi}$  [panel (a)] and Al/ $\text{Co}_2\text{TiGe}$  [panel (b)]. As can be seen, the two systems exhibit a common behavior: the formation energy of the Co-Co terminated interface is smaller for Co-rich conditions ( $\tilde{\mu}$  approaching zero), whereas in Co-poor conditions it is the Ti-Z terminated interface having a smaller energy. In both cases the two lines intersect *below* zero. This means that, in principle, either of the two terminations can be stabilized against Al and  $\text{Co}_2\text{TiZ}$  separation, depending on  $\tilde{\mu}_{\text{Co}}$ , and thus on the growth conditions.

The actual stabilization of a particular interface, on the other hand, will be influenced by the competition with other stable products that may appear during the preparation process. As discussed in Section II C, the upper bound of  $\tilde{\mu}_{\text{Co}}$  is zero, corresponding to the formation of metallic Co. Lower bounds for  $\tilde{\mu}_{\text{Co}}$  can be obtained from Eq. (6) or analogous expressions, assuming the various elements Co, Ti, and Z in thermodynamic equilibrium with competing compounds such as CoTi, TiZ, CoZ. The evaluation of these lower bounds require total energy DFT determinations for the different components in their ground state. For  $Z = \text{Si}$  such calculations were already done by the authors<sup>7</sup> using the current pseudopotentials and exchange-correlation functional. A similar procedure was applied to CoTi (CsCl structure), CoGe ( $B_{20}$  structure), and TiGe ( $B_{27}$  structure). Re-

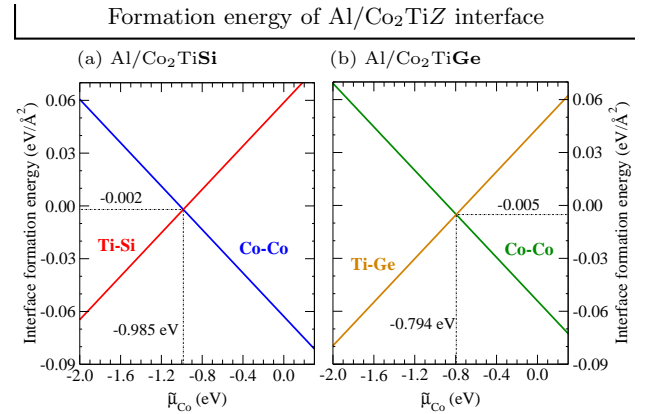


FIG. 5: (Color online) Interface energy for the epitaxial (a) Al/ $\text{Co}_2\text{TiSi}$  and (b) Al/ $\text{Co}_2\text{TiGe}$  interfaces, calculated as a function of the reduced chemical potential of Co,  $\tilde{\mu}_{\text{Co}} = \mu_{\text{Co}} - E_{\text{Co}}$ .

garding the latter, we have searched over several possible structures and found the  $B_{27}$  to have the smallest total energy and being stable against Ti and Ge segregation, in analogy to the TiSi compound.<sup>7</sup>

Taking into account the formation of CoTi, TiZ, and CoZ leads to the following lower bounds of  $\tilde{\mu}_{\text{Co}}$  for the Al/ $\text{Co}_2\text{TiSi}$  interface:

$$\tilde{\mu}_{\text{Co}} \geq \begin{cases} -\tilde{\mu}_{\text{Si}} - 1.83 \text{ eV} & \text{for CoTi} \\ -\tilde{\mu}_{\text{Ti}} - 1.45 \text{ eV} & \text{for CoSi} \\ -0.54 \text{ eV} & \text{for TiSi} \end{cases}, \quad (12)$$

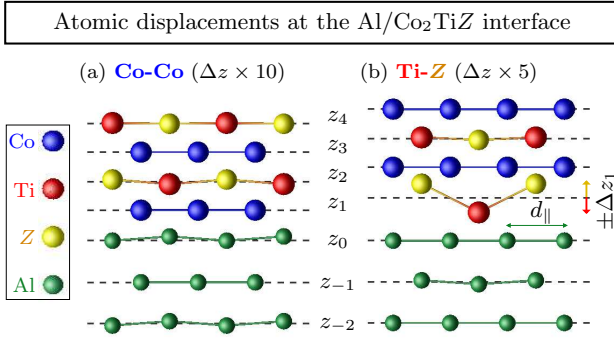


FIG. 6: (Color online) (110)-projected, schematic representations of the inter-atomic distances after accounting for relaxation at the epitaxial Al/Co<sub>2</sub>TiZ interface with (a) Co-Co and (b) Ti-Z terminations, defining the  $z_i$  and  $\Delta z_i$  referred to in text. While the inter-planar and lateral separations are represented on a realistic scale, the atomic vertical displacements are enhanced by a factor  $s = 10$  [panel (a)] or  $s = 5$  [panel (b)], labeled as  $\Delta z \times s$ . One notes a relaxation-induced corrugation of the Ti-Z planes, while the Co-Co planes remain flat. The in-plane inter-atomic distance has a fixed, system-independent value of  $d_{\parallel} = a_0\sqrt{2}/2 = 2.847 \text{ \AA}$ , with  $a_0$  being the equilibrium lattice constant of fcc-Al.

whereas for the Al/Co<sub>2</sub>TiGe interface we obtain

$$\tilde{\mu}_{\text{Co}} \geq \begin{cases} -\tilde{\mu}_{\text{Ge}} - 1.15 \text{ eV} & \text{for CoTi} \\ -\tilde{\mu}_{\text{Ti}} - 1.60 \text{ eV} & \text{for CoGe} \\ -0.52 \text{ eV} & \text{for TiGe} \end{cases} \quad (13)$$

Here, analogous to Co metal,  $\tilde{\mu}_{\text{Ti}}$  and  $\tilde{\mu}_{\text{Z}}$  have zero as upper bounds set by the formation of Ti, Si, and Ge bulk material.

Comparing these values with the Ti-Z/Co-Co crossing points in Fig. 5, it becomes apparent that TiZ spontaneous formation can occur in the range of  $\tilde{\mu}_{\text{Co}}$  where Ti-Z-terminated interfaces are stabilized. Non-equilibrium growth conditions are therefore necessary if such interfaces are desired.

### B. Atomic displacements near the interface

The atomic configurations obtained during the total energy minimization procedure of the interface systems are depicted schematically in Fig. 6. While the two types of Heusler terminations (Co-Co or Ti-Z plane) are expected to be different, both systems considered here, Al/Co<sub>2</sub>TiSi and Al/Co<sub>2</sub>TiGe, share some qualitative features that will be briefly discussed in the following. Quantitative differences in the atomic displacements arise from the different equilibrium bond lengths in the two Heusler materials.

Figure 6 shows the Al/Heusler interface in the immediate vicinity of the contact surface, as seen in a (110)-projection relative to the tetragonal supercell [equivalent to the (100)-direction of the  $L2_1$  structure]. Since each

System:	Al/Co <sub>2</sub> TiSi	Al/Co <sub>2</sub> TiGe
Termination:	Co-Co Ti-Si	Co-Co Ti-Ge
$d_z^{\text{epi}}$	1.455	1.514
$d_4$	1.431 1.468	1.493 1.524
$d_3$	1.478 1.419	1.527 1.470
$d_2$	1.410 1.536	1.498 1.609
$d_1$	1.517 2.120	1.490 2.192
$d_{-1}$	2.071 2.068	2.077 2.056
$d_{-2}$	2.041 2.026	2.047 2.022
$a_0/2$	2.013	

TABLE II: Inter-planar separations (in  $\text{\AA}$ ) for the relaxed epitaxial interfaces Al/Co<sub>2</sub>TiSi and Al/Co<sub>2</sub>TiGe and for the different terminations. The equilibrium inter-planar distances for the epitaxial Heusler alloys ( $d_z^{\text{epi}} = c_{\text{epi}}/4$ ) and for fcc-Al ( $a_0/2$ ) are also given for comparison.

atomic plane contains two inequivalent sites  $A$  and  $B$ , we define the  $z_I$  coordinate of plane  $I$  as the average  $(z_A + z_B)/2$ . Then, the  $z$ -coordinates of sites  $A$  and  $B$  can be given relative to  $z_I$  through the displacement  $\Delta z_I = |z_A - z_B|/2$  as  $z_{A,B} = z_I \pm \Delta z_I$ . The plane coordinates can also be used to define the inter-planar distance between two successive atomic planes as  $d_I = |z_I - z_{I-1}|$ . Relevant values in the vicinity of the interface are listed in Table II. Note that the reference  $z_0 = 0.0$  was taken for the topmost Al-Al plane.

The most important features derived from our calculations can be summarized as follows: (i) while the Co-Co chains remain coplanar, the Ti-Z ones get corrugated. Two successive Co-Co planes can be seen as building a body-centered tetragonal (bct) unit cell in the center of which alternating Ti and Z atoms are placed. In the vicinity of the interface the Ti and Z atoms are being pulled towards the Al substrate, this shift being stronger the closer these atoms are to Al. The maximum displacement is obtained for the first Ti-Z plane,  $\Delta z_1 = 0.14$  or  $0.13 \text{ \AA}$ , for  $Z = \text{Ge}$  or  $\text{Si}$ , respectively. (ii) the Al-Heusler separation strongly depends on the interface termination, but shows only a weak variation with the type of Heusler at a given termination. This quantity corresponds to  $d_1$  in Table II. (iii) at 3–4 monolayers (MLs) away from the interface, slightly varying with the termination, the  $\Delta z$ 's are zero and the inter-planar spacings equal those of the free standing epitaxial Heusler alloy. Here we understand by one ML two successive atomic planes. Table II gives the inter-planar separations up to 2 MLs from the interface. These are compared with the corresponding values in bulk Al ( $a_0/2$ , substrate) and free standing epitaxial Co<sub>2</sub>TiZ ( $d_z^{\text{epi}} = c_{\text{epi}}/4$ ). It can be seen that already within the second ML these values are quite close, leading to the conclusions that (a) deeper Al layers are in the almost perfect fcc structure, and (b) the epitaxial Co<sub>2</sub>TiZ material is distorted only in a very small region near the interface.



### C. Density of states and local spin magnetization

The fast transition to a periodic geometric arrangement along the (001) direction within few MLs away from the interface is also reflected in the electronic structure of the two investigated systems. We illustrate this behavior with the example of the Al/Co<sub>2</sub>TiGe interface, for which we show in Fig. 7(a) and (b) the spin-resolved partial DOS for several atomic planes (each containing two atoms) in the vicinity of the Co-Co [panel (a)] and Ti-Ge [panel (b)] terminated interfaces. The appearance of the minority spin band gap already 3–4 atomic planes away from the interface is easily recognizable in both cases. The same applies for the Co<sub>2</sub>TiSi Heusler alloy which has an even wider band gap.

At the bottom of panels (a) and (b) also the partial DOS of the topmost Al plane is shown. A direct comparison of the Al partial DOS with that of the Co-Co plane seems to indicate a Heusler-substrate hybridization for the Co-Co termination: One notes the peak immediately below  $E_F$  in the majority spin channel and the one above  $E_F$  for the minority spin DOS. A similar pairing is absent for the Ti-Ge terminated interface.

Figure 7(c) displays the local spin magnetic moments, summed up over each atomic plane, across the Al/Co<sub>2</sub>TiZ interface for both terminations. The labeling of the atomic planes follows the same convention as in Fig. 6: The Al plane at the interface has index 0, while all Co<sub>2</sub>TiZ planes have positive indices. We further note that, for the Co-Co (Ti-Z) termination, Co atoms are found in the odd (even) planes. A *very* small spin moment ( $\simeq 0.001 \mu_B$ ) is induced in the substrate, an expected result considering the absence of (partially filled) *d* states in Al. Moreover, also on the Heusler side of the interface the local magnetization is much smaller than that of the inner layers. As expected from the partial DOS, a fast convergence of the local spin magnetic moments with the plane index when moving away from the interface is also obtained.

So far, the combined results of our investigations essentially demonstrate that the effect of the interface on the half-metallicity of the Heusler spacer is quite small and restricted to a very narrow region. When dealing with an Al/Heusler/Al trilayer one can in fact still regard it as a system consisting of a tunneling barrier for minority spin electrons. However, its *effective* thickness is smaller than the *geometric* thickness of the Heusler film. In other words, the physical interface between the two media does not coincide with the 'electronic' interface separating the metallic and the half-metallic character.

This certainly does not rule out other influences that may affect the size or even the very presence of a minority spin band gap in these trilayers. Among these, we mention the effect of spin-orbit coupling on the spin polarization<sup>40</sup> or of the non-quasiparticle states as those found in Co<sub>2</sub>MnSi.<sup>41</sup> While the former can be safely ignored in the considered systems containing relatively light elements, the latter might be important for finite

temperature transport properties.

## V. SPIN-CALORIC EFFECTS

Measurements of the conventional (effective, also called charge) Seebeck coefficient  $S_{\text{eff}}(T)$  have been reported for *bulk* Co<sub>2</sub>TiZ ( $Z = \text{Si, Ge, Sn}$ ) by Barth *et al.*<sup>15</sup> Throughout the whole investigated temperature range it was found to be negative, a typical signature of electron, rather than hole, conduction. Above the Curie temperature  $S_{\text{eff}}(T)$  is constant, with values ranging between  $-31 \mu\text{V/K}$  ( $Z = \text{Si}$ ) and  $-50 \mu\text{V/K}$  ( $Z = \text{Sn}$ ). An analysis of the temperature dependence showed no significant differences between the three systems for  $T \leq 300 \text{ K}$ .<sup>15</sup> This can be seen as a direct consequence of the quite similar electronic structure and magnetic properties of the investigated Heusler alloys.

A completely different situation is expected to occur in the trilayers considered here. First of all, the Heusler spacers are subject to different biaxial strain depending on the group IV element  $Z$ . In addition, we could already see that the type of interface termination leads to different local changes in the structural, electronic, and magnetic properties of the heterostructure. As such, interface scattering is anticipated to influence differently the transmission across the junction, especially for thin Heusler films. We will actually show by using calculations based on Eqs. (10) and (11) that there is a significant dependence of effective and spin-dependent Seebeck coefficients,  $S_{\text{eff}}$  and  $S_{\text{spin}}$ , on both the spacer material and the interface termination. Combined with the results of the previous section on the Al/Heusler interface stability, this is actually equivalent to showing that the spin-caloric properties of these systems can be tuned by targeted epitaxial growth combining the interface morphology with the biaxial strain.

We start by presenting the Seebeck coefficient results for the Al/Co<sub>2</sub>TiZ/Al trilayers. We will then compare them with calculated bulk Seebeck coefficients for the corresponding spacer materials. We close the section by providing a detailed analysis of the transmission probability in the trilayer systems, interpreting the obtained results on the basis of the subtle but significant changes caused to this quantity by the different interface terminations.

### A. Effective and spin-dependent Seebeck coefficients in Al/Co<sub>2</sub>TiZ/Al trilayers

The calculated effective and spin-dependent Seebeck coefficients for the two systems Al/Co<sub>2</sub>TiSi/Al and Al/Co<sub>2</sub>TiGe/Al with different terminations are shown in a compact form in Fig. 8(a) and (b), respectively, for temperatures up to 350 K. Each  $S(T)$  curve is labeled accordingly using a 'spacer (termination)' notation.

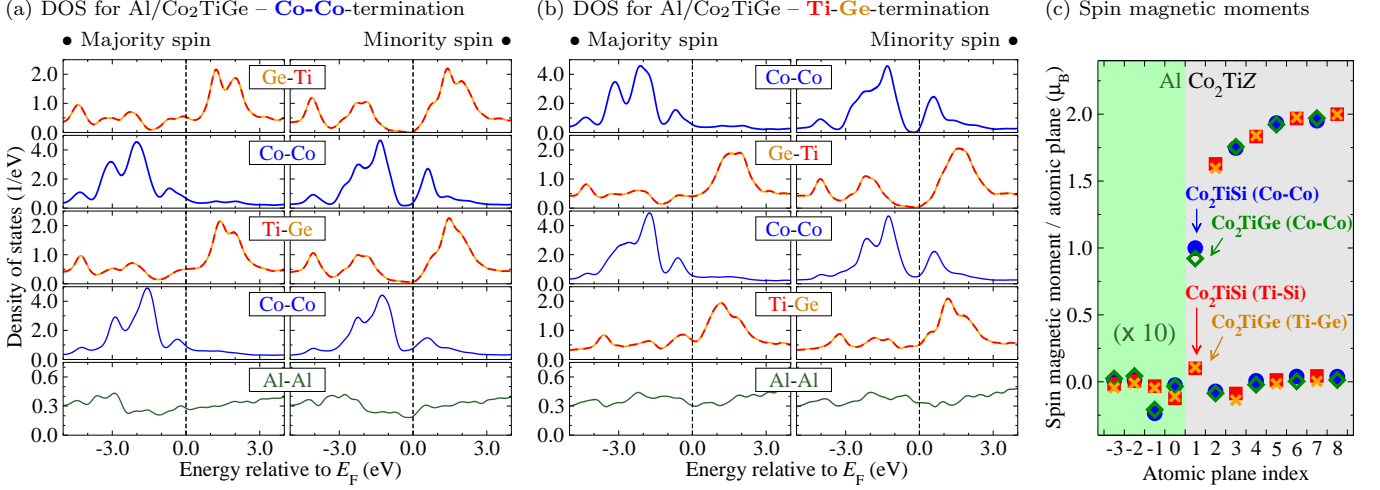


FIG. 7: (Color online) Partial DOS of selected atomic planes in the vicinity of the interface for the Al/Co<sub>2</sub>TiGe system with (a) Co-Co and (b) Ti-Ge termination of the Heusler alloy. (c) Atomic-plane resolved spin magnetic moments at the Al/Co<sub>2</sub>TiZ interface for  $Z = \text{Si/Ge}$  and for both terminations. The index 0 corresponds to the topmost Al plane. Note the factor 10 used to multiply the Al-related data. Co atoms are found in the odd (even) positive index planes when the termination is Co-Co (Ti-Z).

For the effective Seebeck coefficient in Fig. 8(a) it is easy to recognize the following sequence from positive to large negative values: the  $S_{\text{eff}}(T)$  curves for the Ti-Z terminations are above those for Co-Co terminations and the  $Z$  element of the spacer alternates as Si-Ge-Si-Ge. In addition, the different curves do not cross. The Al/Co<sub>2</sub>TiSi/Al system with Co-Co terminated interfaces stands out because of its very small values of both the effective as well as spin-dependent Seebeck coefficient  $S_{\text{spin}}(T)$ . The reason for this peculiar behavior will be made clear below. Concerning the other spacer/termination combinations,  $S_{\text{spin}}(T)$  attains relatively large values as approaching 300 K, being positive for the Ti-Z terminated systems and negative for Al/Co<sub>2</sub>TiGe/Al (Co-Co), as can be seen in Fig. 8(b).

Equations (10) and (11) express the effective and spin-dependent Seebeck coefficients as a weighted sum (difference) of the spin-resolved equivalents  $S_{\sigma}$ , defined by Eq. (9), treating the two spin channels as parallel connected resistors. Although the  $S_{\sigma}$ 's do not have, in a strict sense, a physical meaning, they prove to be useful auxiliary quantities in analyzing  $S_{\text{eff}}$  and  $S_{\text{spin}}$ . We show the calculated  $S_{\uparrow}(T)$  (majority spin) and  $S_{\downarrow}(T)$  (minority spin) in Fig. 9(a) and (b), where we have used the same spacer/termination labeling convention as above.

As can be seen, except for the Al/Co<sub>2</sub>TiGe/Al (Ti-Ge) system,  $S_{\uparrow}(T)$  and  $S_{\downarrow}(T)$  are of different sign over the whole temperature range. Regarding the Seebeck coefficient as a potential drop, this would correspond to electrons of different spin moving in opposite directions across the junction. A direct comparison of the (a) panels of Fig. 8 and Fig. 9 reveals that  $S_{\text{eff}}$  is mainly determined by  $S_{\uparrow}$ : the same sequence from positive to neg-

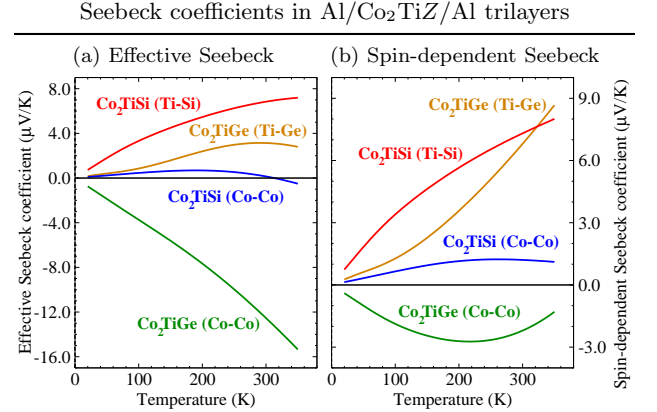


FIG. 8: (Color online) (a) Effective and (b) spin-dependent Seebeck coefficients calculated according to Eqs. (10) and (11) for the Al/Co<sub>2</sub>TiSi/Al and Al/Co<sub>2</sub>TiGe/Al trilayer systems. The labeling of the curves designates the respective spacer material and Al-Heusler interface termination (Co-Co or Ti-Z) in parentheses.

ative values in the temperature dependence appears in both  $S_{\uparrow}$  and in  $S_{\text{eff}}$ . The minority spin component  $S_{\downarrow}$ , in turn, exhibits a fairly similar  $T$ -dependence regardless of spacer and termination. Recall that a band gap is present in the minority spin channel, rendering the spin-down transmission into a 'tunneling through a semiconductor'-equivalent case. Since  $S_{\downarrow}$  is weighted with the minority spin conductance  $G_{\downarrow}$  in Eqs. (10) and (11), this explains why its contribution to both  $S_{\text{eff}}$  and  $S_{\text{spin}}$ , in spite of the very large values, is drastically diminished.

A deeper insight into the peculiarities of the Seebeck

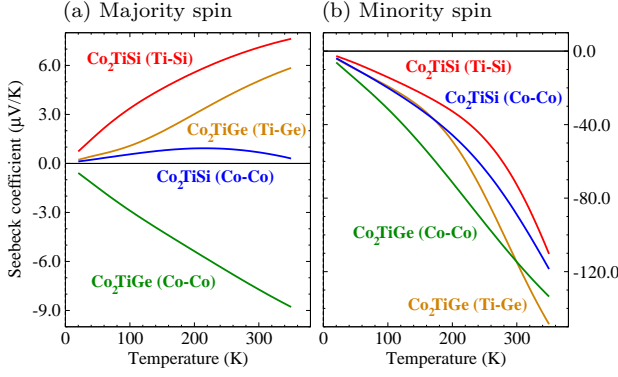
Spin-resolved Seebeck coefficients in Al/Co<sub>2</sub>TiZ/Al

FIG. 9: (Color online) Spin-resolved Seebeck coefficients, defined by Eq. (9), for (a) majority spin and (b) minority spin channels calculated for the Al/Co<sub>2</sub>TiSi/Al and Al/Co<sub>2</sub>TiGe/Al trilayer systems. The labeling of the curves follows the same convention as Fig. 8. Note the different scales on the  $y$ -axis used in the two panels.

coefficients is provided by the electronic transmission probability  $\mathcal{T}_\sigma(E)$  defined by Eq. (7), which lies at the core of the transport calculations. The way in which a specific transmission probability profile  $\mathcal{T}(E)$  influences the sign and size of the Seebeck coefficient can be explained in a very intuitive manner on the basis of Eq. (9).<sup>42</sup> The denominator of  $S(T)$  in this formula (spin index omitted) is proportional to the conductance  $G(T)$ , as given by Eq. (8). Because of the  $(E - E_F)$  term, the numerator may be seen as a center of mass of  $\mathcal{T}(E)(\partial f_0/\partial E)$ .<sup>42</sup> Consequently, both sign and value of  $S(T)$  will be extremely sensitive to small changes in the numerator's integrand below or above  $E_F$ . These changes are brought upon by the temperature increase which extends the effective non-zero width of  $\mathcal{T}(E)(\partial f_0/\partial E)$ . This interpretation is equivalent to Mott's formula<sup>27</sup> in the limit of  $T \rightarrow 0$ ; that is,  $S$  is proportional to the logarithmic derivative of the conductivity at  $E_F$ , its sign being positive (negative) for a negative (positive) slope of  $\sigma(E)$ .

The transmission probability curves calculated using Eq. (7) are shown for Al/Co<sub>2</sub>TiSi/Al and Al/Co<sub>2</sub>TiGe/Al in Fig. 10(a) and (b), respectively, resolved according to the majority (top) and minority (bottom) spin channels.

The aforementioned gap in the minority spin channel (bottom panels) is correspondingly reflected in the transmission probability as a broad energy interval around  $E_F$  where  $\mathcal{T}_\downarrow(E) \rightarrow 0$ . Above the Fermi energy a sudden increase follows, with the onset higher for Al/Co<sub>2</sub>TiSi/Al than for Al/Co<sub>2</sub>TiGe/Al. This is due to the stronger tetragonal distortion in the latter case, effectively leading to a much smaller band gap in the strained Co<sub>2</sub>TiGe spacer. Since in all cases the transmission switches from zero, below  $E_F$ , to a finite value above it,  $S_\downarrow(T)$  must necessarily be negative. Striking differences in the trans-

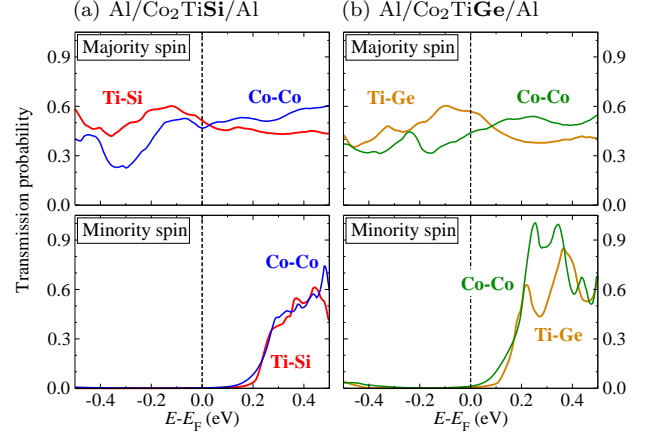
Transmission probability in Al/Co<sub>2</sub>TiZ/Al

FIG. 10: (Color online) Spin-resolved electronic transmission probability calculated for (a) Al/Co<sub>2</sub>TiSi/Al and (b) Al/Co<sub>2</sub>TiGe/Al heterostructures. For each system and spin component one panel contains two sets of data corresponding to the different terminations, Co-Co or Ti-Z, of the Heusler-Al interface, appropriately labeled.

mission for the two terminations can be observed only in the Co<sub>2</sub>TiGe-based system. Their energy position is nevertheless quite high above the Fermi energy and, because of the rapid decay of  $(\partial f_0/\partial E)$ , have no influence on the Seebeck coefficient.

In the majority spin channel (upper panels) the expected differences in the transmission between the two terminations Co-Co and Ti-Z are clearly visible for both spacers. It is, however, important to note that  $\mathcal{T}_\uparrow(E)$  for the Ti-Z terminations are quite similar in shape: both have a broad peak right below  $E_F$  which thus lies on a negative slope flank of  $\mathcal{T}_\uparrow(E)$ . These features explain the positive sign and the close values obtained in  $S_\uparrow$ ,  $S_{\text{eff}}$ , and  $S_{\text{spin}}$  for both Ti-Z trilayers. In contrast, the Co-Co terminations for the two spacer materials show very different transmission profiles: In Al/Co<sub>2</sub>TiSi/Al,  $\mathcal{T}_\uparrow(E)$  is nearly constant around  $E_F$ , exhibiting only weak oscillations. The Fermi energy itself lies in the middle of a rather symmetric dip in the transmission, which provides the reason for the small Seebeck coefficients  $S_\uparrow$ ,  $S_{\text{eff}}$ , and  $S_{\text{spin}}$  obtained for (Co-Co)-Al/Co<sub>2</sub>TiSi/Al. For the other spacer material, Co<sub>2</sub>TiGe, the maximum in transmission lies above  $E_F$ , which is thus on a positive slope flank of  $\mathcal{T}_\uparrow(E)$ , and so all the above coefficients are negative.

## B. Transport properties of bulk Co<sub>2</sub>TiZ

We have analyzed in Section III the electronic structure of the bulk Co<sub>2</sub>TiZ Heusler alloys, in particular the free standing epitaxial systems matched to Al(001), with the purpose of identifying specific bulk characteristics in the electronic structure of the trilayer systems. We follow here a similar path and show results obtained for the

transmission probability and the effective Seebeck coefficient for the bulk systems.

We derive these results within our approach by studying a fictitious trilayer system having the left and right leads, as well as the spacer in between, consisting of identical materials. For each transmission channel  $\vec{k}_{\parallel}$  the transmission  $\mathcal{T}(\vec{k}_{\parallel}, E)$  is a well-defined quantity, being proportional to the  $\vec{k}_{\parallel}$ -projected  $E(\vec{k}) = E(\vec{k}_{\parallel}, k_z)$  isosurface.<sup>43</sup> For example, the quantity  $\mathcal{T}(\vec{k}_{\parallel}, E_F)$  will represent the Fermi surface projected on the  $(k_x, k_y)$ -plane.

Such a construction allows one to isolate in the transmission curves precisely those states involved that come solely from the (appropriately strained) spacer material without any influence of the interfaces. A one-to-one comparison with transmission profiles for the true trilayer system is also possible, if the outgoing/receiving states of the left/right leads match, to some extent, those of the spacer.

Corresponding results obtained for bulk  $\text{Co}_2\text{TiSi}$  and  $\text{Co}_2\text{TiGe}$  are displayed in Fig. 11. Panels (a) of this figure show the spin-resolved electronic transmission, while panels (b) show the effective Seebeck coefficient. In each case, a comparison is made between the ideal  $L2_1$  structure of the respective Heusler alloy [thin light blue (grey) lines] and its tetragonally distorted, Al(001) epitaxially matched structure [thick dark red (grey) lines].

A side-by-side comparison between  $\text{Co}_2\text{TiSi}$  (left) and  $\text{Co}_2\text{TiGe}$  (right) results for the  $L2_1$  structure reveals no significant differences, neither in the transmission profiles, nor in the Seebeck coefficients. The obvious reason is the same as mentioned above for the experimental data: the fairly identical electronic structure of the two materials.

Our results for the effective Seebeck coefficient of the  $L2_1$   $\text{Co}_2\text{TiZ}$  Heusler alloys agree well with previous calculations based on solving the Boltzmann equation.<sup>15,32</sup> Under epitaxial conditions, we note that a change in  $S(T)$  occurs only for  $\text{Co}_2\text{TiGe}$ , Fig. 11(b), right panel. Only for this compound does the Fermi energy come close enough to the conduction band such that, for finite but not exceedingly high temperatures, the minority spin transmission and conductance becomes finite. As a consequence, the semiconductor-like minority spin current  $G_{\downarrow}S_{\downarrow}$  shows up in the numerator of the effective Seebeck coefficient, Eq. (10), leading to the occurrence of large, negative values.

We turn back to the transmission profiles, Fig. 11(a), and note that, for the tetragonally distorted (epitaxial) systems, the transmission changes to a different extent in the two Heusler materials because of the different biaxial strain and outward expansion. The effect is clearly stronger for  $\text{Co}_2\text{TiGe}$ , as one can see in the more pronounced shift of the minority spin transmission towards lower energies. In fact, comparing the onsets of minority spin transmission for the tetragonal  $\text{Co}_2\text{TiSi}$  and  $\text{Co}_2\text{TiGe}$  with the corresponding onsets in the trilayer

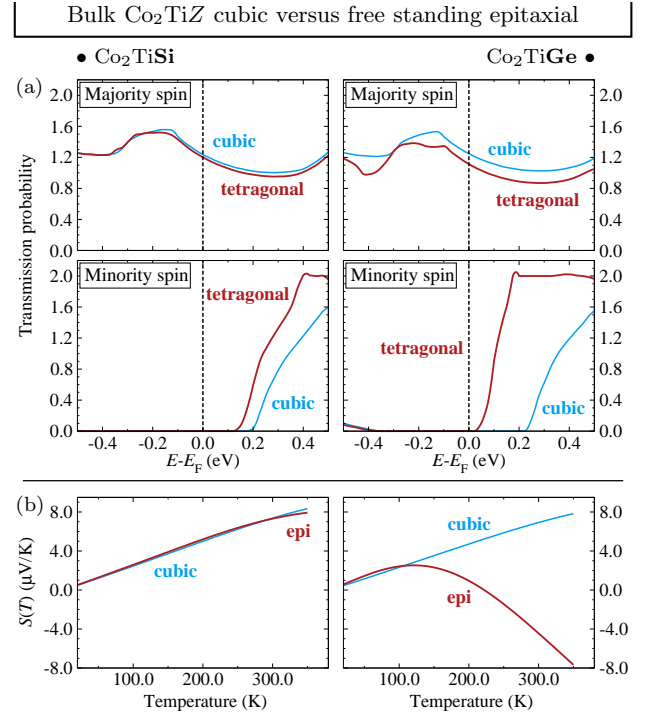


FIG. 11: (Color online) (a) Spin-resolved electronic transmission probability and (b) effective Seebeck coefficient calculated for *bulk*  $\text{Co}_2\text{TiSi}$  and  $\text{Co}_2\text{TiGe}$ . Each panel shows two sets of data, one corresponding to the  $L2_1$  (cubic) Heusler structure (thin light blue/grey), the second to the tetragonally distorted structure, epitaxially matched to fcc-Al (thick dark red/grey).

systems in Fig. 10 we note that they match nearly perfectly. The small differences appear because of (i) different reference Fermi energies of the leads and (ii) the tails in  $\mathcal{T}_{\downarrow}(E)$  caused by the evanescent states at the Al/Heusler interfaces. It is further important to note, by comparing  $\mathcal{T}_{\downarrow}(E)$  with the band structure of  $\text{Co}_2\text{TiGe}$  in Fig. 4, that the downwards shift in  $\mathcal{T}_{\downarrow}(E)$  has a one-to-one correspondence in the similar shift of the minority spin bands under epitaxial distortion. This proves once more that, even at this small thickness of the spacer materials in Al/ $\text{Co}_2\text{TiZ}$ /Al trilayers, the former do act as efficient potential barriers for the spin-down electrons by preserving their half-metallic character.

We make a final observation regarding the transmission in the majority spin channel for both  $\text{Co}_2\text{TiSi}$  and  $\text{Co}_2\text{TiGe}$ . The two bulk profiles are fairly similar to those of the Ti-Z-terminated trilayers. In both the free tetragonal spacers and the heterojunction a broad peak is present below the Fermi energy, followed by a falling transmission above it. This has to be contrasted with the completely different pattern of  $\mathcal{T}_{\uparrow}$  in the Co-Co terminated trilayers. In Section IV we have shown two important differences between the two types of terminations for a given spacer material: (i) the Co-Co-terminated Heusler alloy is much closer to the Al substrate than

the Ti-Z-terminated, and (ii) the partial DOS curves indicate a Heusler/Al hybridization at the interface only in the case of a Co-Co-termination. The clearly different Seebeck coefficients and transmission profiles for the two terminations appear to be linked precisely to these features. We shall investigate in the following the even more subtle differences in the  $\vec{k}_{\parallel}$ -dependence of the transmission probability caused by the interface morphology. Moreover, we show how the interplay between strain and  $\vec{k}_{\parallel}$  selectivity leads to quite different results even for the same termination, but with a different spacer material.

### C. The influence of the Al/Co<sub>2</sub>TiZ interface on the transmission probability

The transmission probability curves discussed so far were analyzed in their energy dependence. It is of interest at this point to go one step back and investigate, at selected energy arguments of Eq. (7), the individual contributions of the  $\vec{k}_{\parallel}$  transmission channels in the two-dimensional (2D) BZ. This proves useful in identifying which of these channels are actually involved in transmission and to what extent they change from one trilayer system to another.

We show in Fig. 12 contour plots of  $\mathcal{T}_{\sigma}(\vec{k}_{\parallel}, E)$  for  $E = E_F$ , in the full 2D-BZ and for all combinations spacer material-interface termination studied here. We have used in this figure a common scale for all panels. For this reason, an enhancement factor of 20 has been applied to the minority spin channel transmission in Fig. 12 (b). The  $k_x$  and  $k_y$  axes of the 2D reciprocal space are orthogonal to each other, pointing along the horizontal and vertical sides of each panel, positioned in such a way that its center coincides with the  $\bar{\Gamma}$ -point of the 2D-BZ.

While rows (a) and (b) of Fig. 12 naturally separate the transmission probability according to the spin components, the panels belonging to a certain spacer-termination combination have been grouped in such a way as to emphasize the similarities in  $\mathcal{T}_{\sigma}(E)$  discussed above.

The latter is particularly easy to recognize in the minority spin channel: for the Ti-Z terminated interfaces (left column) the map of Al/Co<sub>2</sub>TiGe/Al (right frame) is seen to be identical in shape with that of Al/Co<sub>2</sub>TiSi/Al (left frame) and differing only in the amplitude of the transmission at various  $\vec{k}_{\parallel}$  points, reflected by the different color. A similar correspondence can be seen for the Co-Co terminated systems in the right column of Fig. 12(b). As anticipated from the  $\mathcal{T}_{\downarrow}(E)$  transmission profiles in Fig. 10, the  $\mathcal{T}_{\downarrow}(E, \vec{k}_{\parallel})$  plots bear the typical characteristics of tunneling: very few transmission channels, mostly oriented along  $k_x$  and  $k_y$  and placed near the 2D-BZ center (close to normal incidence), do participate in the transmission. On the other hand, comparison of the frames corresponding to identical spacer, e.g., Co<sub>2</sub>TiGe, but different terminations, shows clear quali-

tative differences in the transmission which are caused by the nature of the Al/Heusler contact.

In the majority spin channel, Fig. 12(a), we find a similar pattern for the two Ti-Z terminations: the different spacer materials change only the amplitude in transmission, but do not introduce or remove any individual transmission channels. This is directly reflected in the two transmission profiles  $\mathcal{T}_{\uparrow}(E)$  (Fig. 10) and the Seebeck coefficients calculated for the Ti-Z terminations (Fig. 9) that were found to share the same qualitative energy and temperature dependence.

A completely different situation is encountered for the Co-Co terminated Al/Co<sub>2</sub>TiZ/Al trilayers in the majority spin channel, Fig. 12(a), right column. While the transmission at  $E_F$  for the Co<sub>2</sub>TiGe spacer shows large contributions near  $\vec{k}_{\parallel} = \bar{\Gamma}$  (corresponding to normal incidence), these channels are almost blocked for Co<sub>2</sub>TiSi (the dark blue area around  $\bar{\Gamma}$ ). In turn, Co<sub>2</sub>TiSi favors transmission channels along the diagonals of the 2D-BZ far from  $\bar{\Gamma}$  which appear very weak in Co<sub>2</sub>TiGe. The absence of these transmission channels around the zone center is precisely the reason for the peculiar characteristics of  $\mathcal{T}_{\uparrow}(E)$  and thus of  $S_{\uparrow}(T)$ ,  $S_{\text{eff}}(T)$ , and  $S_{\text{spin}}(T)$  evidenced above.

Figure 13 displays similar contour plots, but now focusing only on the majority spin channel and tracing the evolution of  $\mathcal{T}_{\uparrow}(\vec{k}_{\parallel}, E)$  for several energy arguments,  $E_F - 90$  meV,  $E_F$ , and  $E_F + 90$  meV. The layout of this figure is similar to that of Fig. 12 (Ti-Z-terminated systems on the left and Co-Co-terminated on the right), but we have also added the transmission maps of bulk Al leads. They represent the incoming/receiving available transmission channels and correspond to the transmission maps which would be obtained if the spacers were absent. The map for  $E = E_F$  is equivalent to the projected Fermi surface of Al.

The main point we wanted to make by this energy-dependent side-by-side comparison is that transmission channels near  $\bar{\Gamma}$  are available over the whole relevant energy range. Moreover, taking just Al bulk, the intensity and width of the transmission around the zone center is expected to increase. As can be seen, the Al/Co<sub>2</sub>TiSi/Al trilayer with Co-Co termination lacks such transmission channels for *all* energy arguments. At higher energies, here at  $E_F + 90$  meV, they start to weaken also for Al/Co<sub>2</sub>TiGe/Al with Co-Co termination. The Ti-Z terminated systems, on the other hand, share qualitatively similar features, with small quantitative differences, over a wide energy range.

## VI. SUMMARY

We have investigated the structural stability and the potential applicability as thermally driven spin injectors of heterojunctions consisting of Al(001) and thin films of the closely lattice-matched Heusler alloys Co<sub>2</sub>TiSi and Co<sub>2</sub>TiGe. Our most important findings can be summa-



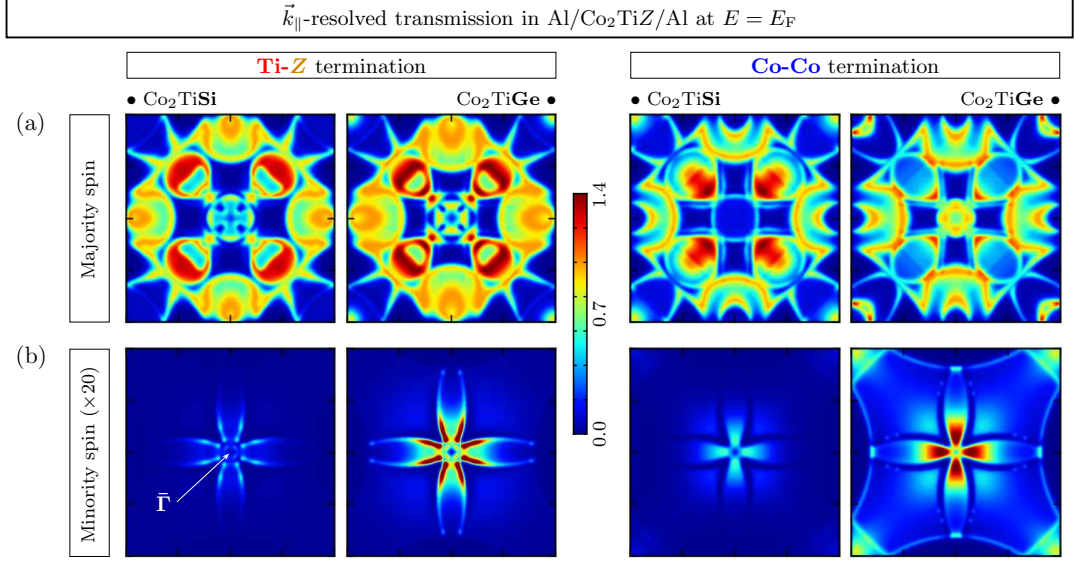


FIG. 12: (Color online) Contour plots of the  $\vec{k}_{\parallel}$ -resolved transmission probability in Al/Co<sub>2</sub>TiZ/Al as calculated for the energy argument  $E = E_F$ . Rows (a) and (b) show respectively the majority and minority spin channels. Left (right) columns correspond to the Ti-Z (Co-Co) terminated Al/Co<sub>2</sub>TiZ interface. The BZ center is in the middle of each square, as indicated by the  $\bar{\Gamma}$  point in the bottom left panel. The  $k_x$  ( $k_y$ ) axis has horizontal (vertical) orientation.

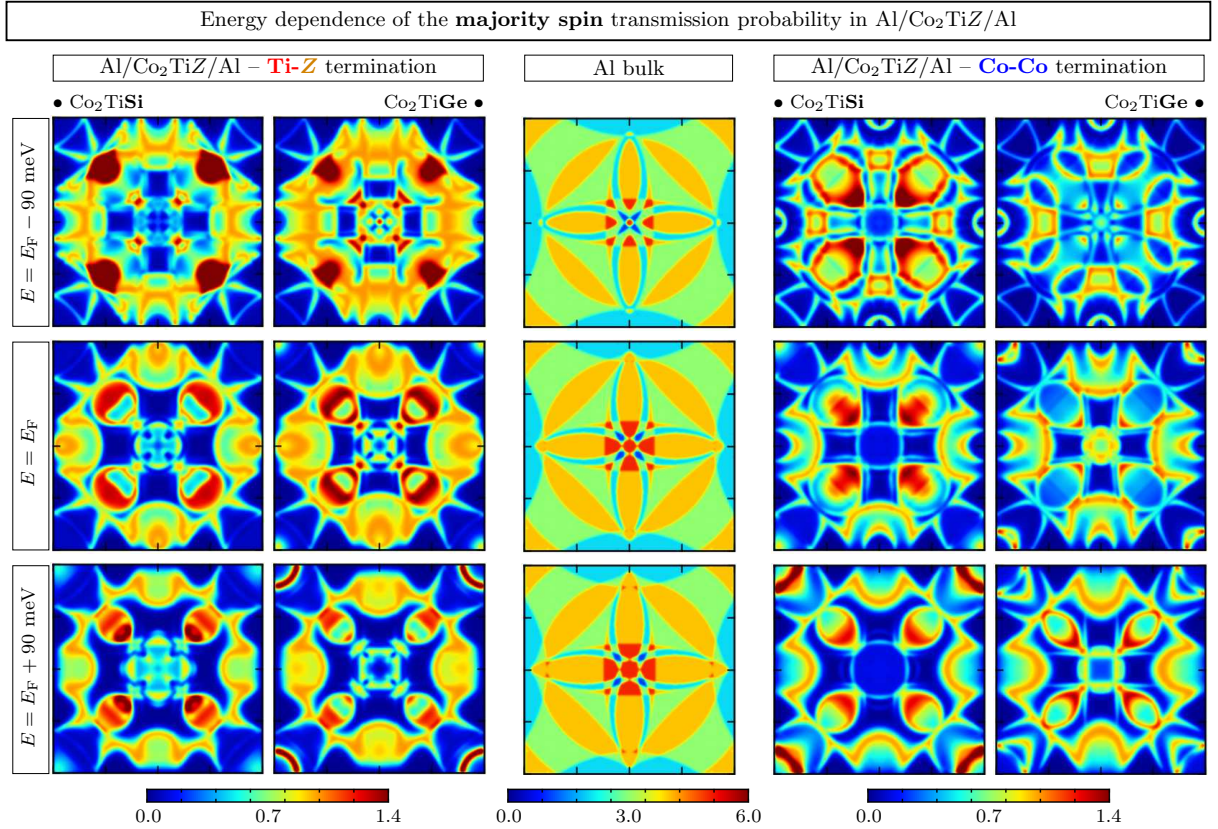


FIG. 13: (Color online) Contour plots of the majority spin  $\vec{k}_{\parallel}$ -resolved transmission probability in Al/Co<sub>2</sub>TiZ/Al for various energy arguments:  $E = E_F - 90$  meV,  $E = E_F$ , and  $E = E_F + 90$  meV, from top to bottom. The left (right) columns correspond to the Ti-Z (Co-Co) terminated Al/Co<sub>2</sub>TiZ interface. The middle column shows (on a different scale) the transmission through unstrained Al bulk. The BZ is identical to that of Fig. 12.



rized as follows:

(i) The Al structure can be continued by Heusler alloys terminated either by Co-Co or Ti- $Z$  ( $Z = \text{Si}$  or  $\text{Ge}$ ) planes; *ab initio* thermodynamic calculations predict that both terminations are stable against Al and  $\text{Co}_2\text{TiZ}$  separation. Formation of Ti- $Z$ -terminated interfaces require, however, out-of-equilibrium growth conditions.

(ii) As a consequence of a smaller equilibrium Co-Al bond length than Ti-Al or Si(Ge)-Al, the structural relaxation occurring at the interface leads to a smaller separation between Al and the Heusler alloy spacer in the case of a Co-Co terminated interface. This configuration appears to favor the Co-Al hybridization across the interface.

(iii) The small lattice mismatch between the two components (Al and Heusler alloy) results in a sharp localization of the interface specific distortions, both morphologic and in the electronic structure. Within 3 – 4 MLs away from the interface the Heusler alloys accommodate an epitaxial, tetragonally distorted structure, with a preserved half-metallicity. The systems can be still regarded as metal/half-metal heterojunction, but the effective thickness of the half-metallic spacer is smaller than the geometric thickness of the Heusler film.

(iv) The effective and spin-dependent Seebeck coefficients significantly depend on the particular spacer/termination combination. Combined with the growth conditions dependence of the formation of a specific stable interface, this establishes a direct connection between growth and spin-caloric properties control in these samples.

(v) The Ti- $Z$ -terminated trilayers exhibit qualita-

tive similar features with slight quantitative differences caused by varying the group IV element  $Z$ . In both cases, the spin-dependent Seebeck coefficient is predicted to be large, actually of the same size as the effective Seebeck coefficient. This practically means that nearly the entire voltage generated under a temperature gradient is converted into spin accumulation!

(vi) The Co-Co terminated systems are characterized by large quantitative *and* qualitative differences. In particular, we could show that, by strongly reducing the transmission through the normal incidence channels, the Co-Co terminated Al/ $\text{Co}_2\text{TiSi}$ /Al heterojunction exhibits a much weaker energy dependence of transmission and thus a much smaller (effective and spin-dependent) Seebeck coefficient.

### Acknowledgments

This work was supported by the German Research Foundation (*Deutsche Forschungsgemeinschaft – DFG*) within the Priority Program 1538 "Spin Caloric Transport (SpinCaT)". The authors gratefully acknowledge the computing time granted by the John von Neumann Institute for Computing (NIC) and provided on the supercomputer JUROPA at Jülich Supercomputing Centre (JSC). Additional computer facilities have been offered by the Center for Computational Sciences and Simulation (CCSS) at the University Duisburg-Essen. We also thank Phivos Mavropoulos for enlightening discussions on the Landauer-Büttiker formalism.

---

\* E-mail: voicu.popescu@uni-due.de

<sup>1</sup> I. Žutić, J. Fabian, and S. Das Sarma, *Rev. Mod. Phys.* **76**, 323 (2004).

<sup>2</sup> R. Jansen, *Nat. Mater.* **11**, 400 (2012).

<sup>3</sup> P. A. Bennett, D. J. Smith, and I. K. Robinson, *Applied Surface Science* **180**, 65 (2001).

<sup>4</sup> M. Krause, F. Blobner, L. Hammer, K. Heinz, and U. Starke, *Phys. Rev. B* **68**, 125306 (2003).

<sup>5</sup> H. Wu, P. Kratzer, and M. Scheffler, *Phys. Rev. B* **72**, 144425 (2005).

<sup>6</sup> B. Geisler, P. Kratzer, T. Suzuki, T. Lutz, G. Costantini, and K. Kern, *Phys. Rev. B* **86**, 115428 (2012).

<sup>7</sup> B. Geisler and P. Kratzer, *Phys. Rev. B* **88**, 115433 (2013).

<sup>8</sup> H. C. Card, *IEEE Transactions on Electron Devices* **23**, 538 (1976).

<sup>9</sup> J. Fabian and S. Das Sarma, *Phys. Rev. Lett.* **83**, 1211 (1999).

<sup>10</sup> S. Chadov, T. Graf, K. Chadova, X. Dai, F. Casper, G. H. Fecher, and C. Felser, *Phys. Rev. Lett.* **107**, 047202 (2011).

<sup>11</sup> H. C. Kandpal, G. H. Fecher, and C. Felser, *Journal of Physics D: Applied Physics* **40**, 1507 (2007).

<sup>12</sup> G. Schmidt, D. Ferrand, L. W. Molenkamp, A. T. Filip, and B. J. van Wees, *Phys. Rev. B* **62**, 4790 (2000).

<sup>13</sup> A. Slachter, F. L. Bakker, J. P. Adam, and B. J. van Wees,

*Nature Physics* **6**, 879 (2010).

<sup>14</sup> B. Balke, S. Ouardi, T. Graf, J. Barth, C. G. Blum, G. H. Fecher, A. Shkabko, A. Weidenkaff, and C. Felser, *Solid St. Comm.* **150**, 529 (2010).

<sup>15</sup> J. Barth, G. H. Fecher, B. Balke, S. Ouardi, T. Graf, C. Felser, A. Shkabko, A. Weidenkaff, P. Klaer, H. J. Elmers, et al., *Phys. Rev. B* **81**, 064404 (2010).

<sup>16</sup> T. Graf, C. Felser, and S. S. Parkin, *Progress in Solid State Chemistry* **39**, 1 (2011).

<sup>17</sup> P. Giannozzi, S. Baroni, N. Bonini, M. Calandra, R. Car, C. Cavazzoni, D. Ceresoli, G. L. Chiarotti, M. Cococcioni, I. Dabo, et al., *J. Phys. Cond. Matter* **21**, 395502 (2009).

<sup>18</sup> J. P. Perdew, K. Burke, and M. Ernzerhof, *Phys. Rev. Lett.* **77**, 3865 (1996).

<sup>19</sup> D. Vanderbilt, *Phys. Rev. B* **41**, 7892 (1990).

<sup>20</sup> For Al, we used the Al.pbe-n-van.UPF pseudopotential from <http://www.quantum-espresso.org>.

<sup>21</sup> S. G. Louie, S. Froyen, and M. L. Cohen, *Phys. Rev. B* **26**, 1738 (1982).

<sup>22</sup> M. Methfessel and A. T. Paxton, *Phys. Rev. B* **40**, 3616 (1989).

<sup>23</sup> H. J. Monkhorst and J. D. Pack, *Phys. Rev. B* **13**, 5188 (1976).

<sup>24</sup> K. Reuter, C. Stampfl, and M. Scheffler, *Handbook of Ma-*

- terials Modeling* (Kluwer, Dordrecht, The Netherlands, 2004), chap. Ab Initio Atomistic Thermodynamics and Statistical Mechanics of Surface Properties and Functions.
- <sup>25</sup> A. Smogunov, A. Dal Corso, and E. Tosatti, Phys. Rev. B **70**, 045417 (2004).
  - <sup>26</sup> H. Joon Choi and J. Ihm, Phys. Rev. B **59**, 2267 (1999).
  - <sup>27</sup> U. Sivan and Y. Imry, Phys. Rev. B **33**, 551 (1986).
  - <sup>28</sup> A. L. Wysocki, R. F. Sabirianov, M. van Schilfgaarde, and K. D. Belashchenko, Phys. Rev. B **80**, 224423 (2009).
  - <sup>29</sup> J. Kudrnovský, V. Drchal, I. Turek, S. Khmelevskiy, J. K. Glasbrenner, and K. D. Belashchenko, Phys. Rev. B **86**, 144423 (2012).
  - <sup>30</sup> R. Kováčik, P. Mavropoulos, D. Wortmann, and S. Blügel, ArXiv e-prints (2014), 1401.6939.
  - <sup>31</sup> S. C. Lee, T. D. Lee, P. Blaha, and K. Schwarz, Journal of Applied Physics **97**, 10C307 (2005).
  - <sup>32</sup> V. Sharma, A. K. Solanki, and A. Kashyap, J. Magn. Magn. Mat. **322**, 2922 (2010).
  - <sup>33</sup> P. J. Webster and K. R. A. Ziebeck, J. Phys. Chem. Solids **34**, 1647 (1973).
  - <sup>34</sup> A. W. Carbonari, W. Pendl Jr., R. N. Attili, and R. N. Saxena, Hyperfine Interactions **80**, 971 (1993).
  - <sup>35</sup> J. Kudrnovský, V. Drchal, and I. Turek, Phys. Rev. B **88**, 014422 (2013).
  - <sup>36</sup> M. Meinert, J.-M. Schmalhorst, and G. Reiss, Applied Physics Letters **97**, 012501 (2010).
  - <sup>37</sup> When using an 8-atom tetragonal unit cell of height  $c = a_0\sqrt{2}$  the folded  $Z$ -point of the fcc BZ does not fall halfway between the  $\Gamma$  and  $Z$  points of the tetragonal BZ in Fig. 4. The same applies to the  $X$ - $R$  and  $M$ - $A$  directions.
  - <sup>38</sup> W. Setyawan and S. Curtarolo, Computational Materials Science **49**, 299 (2010).
  - <sup>39</sup> B. Hülsen, M. Scheffler, and P. Kratzer, Phys. Rev. Lett. **103**, 046802 (2009).
  - <sup>40</sup> P. Mavropoulos, K. Sato, R. Zeller, P. H. Dederichs, V. Popescu, and H. Ebert, Phys. Rev. B **69**, 054424 (2004).
  - <sup>41</sup> L. Chioncel, Y. Sakuraba, E. Arrigoni, M. I. Katsnelson, M. Oogane, Y. Ando, T. Miyazaki, E. Burzo, and A. I. Lichtenstein, Phys. Rev. Lett. **100**, 086402 (2008).
  - <sup>42</sup> M. Czerner, M. Bachmann, and C. Heiliger, Phys. Rev. B **83**, 132405 (2011).
  - <sup>43</sup> P. Mavropoulos, N. Papanikolaou, and P. H. Dederichs, Phys. Rev. B **69**, 125104 (2004).